

# Shock generated vorticity in spark discharges

Bhavini Singh<sup>1</sup>, L.K. Rajendran<sup>1</sup>, P.P.Vlachos<sup>2</sup>, and S.P.M. Bane<sup>1</sup>†

<sup>1</sup>School of Aeronautics and Astronautics, Purdue University, West Lafayette, Indiana 47907, USA

<sup>2</sup>School of Mechanical Engineering, Purdue University, West Lafayette, Indiana 47907, USA

(Received xx; revised xx; accepted xx)

Spark discharges induce a complex flow field consisting of a shock wave at early times ( $\sim 1 \mu\text{s}$ ), a pair of vortex rings, and a hot gas kernel. In this work, we investigate the shock wave's role in producing the vortex ring vorticity. We analyze high-speed (700 kHz) schlieren images of the shock wave for a range of electrical energies to measure the shock properties and estimate shock velocity and curvature. These measurements are combined with a model to calculate the vorticity generated. The measurements show that the highest vorticity is generated near the peak shock curvature location, and the shock curvature and strength increase with electrical energy deposited. A comparison of the vorticity estimated from the model to vorticity measurements from stereoscopic particle image velocimetry shows the results to be statistically equivalent. This suggests that the vorticity induced by spark discharges may be approximated from the shock curvature and velocity and that their magnitudes control the strength and location of the induced vortex rings which drive the cooling and mixing of the hot gas kernel.

## 1. Introduction

Spark plasma discharges lead to rapid heating and pressure rise in the electrode gap, resulting in a shock wave (Raizer, Yuri 1991). The shock wave moves radially out of the center of the gap within a few microseconds (Bane *et al.* 2015) and decays rapidly into an acoustic wave. After the shock wave departure, the flow field is comprised of a hot gas kernel and vortex ring(s). The number of vortex rings, their dynamics, and the hot gas kernel evolution depend on the spark generation method (Singh *et al.* 2020a; Wang *et al.* 2020; Rajendran *et al.* 2020). In laser sparks, for instance, a pair of vortex rings of unequal strength and size are induced (Wang *et al.* 2020; Dumitrache & Yalin 2020), while in sparks generated between cone-tipped electrodes (pin-to-pin discharges), a pair of two almost identical vortex rings are induced (Singh *et al.* 2018, 2020a,b) and in surface discharges, a single vortex ring is formed that propagates away from the discharge surface (Rajendran *et al.* 2020).

In these cases, the strength and dynamics of the vortex ring(s) control the spatial extent and cooling of the hot gas kernel and thus play a critical role in engineering applications. In laser sparks, which are typically used for combustion applications, the vortex ring characteristics control the direction and ejection of the hot gas kernel (Wang *et al.* 2020), affecting ignition and flame growth (Phuoc 2006). In pin-to-pin electrical spark discharges, the rings entrain cold ambient gas into the hot kernel to promote rapid cooling/mixing, and this determines

† Email address for correspondence: sbane@purdue.edu



the required pulsation frequency of the discharges to utilize the synergetic effect of multiple pulses to optimize ignition systems (Lefkowitz & Ombrello 2017) or to stabilize flames and promote efficient combustion (Pilla *et al.* 2008).

Despite the critical role vortex rings play in the flow induced by spark discharges, there has been little experimental investigation on the source of this vorticity. Researchers have used CFD simulations to study the induced flow and suggested that the non-uniformity in the shock strength may be the source of vorticity in the sparks through a baroclinic effect (Picone & Boris 1983; Singh *et al.* 2019; Dumitrache *et al.* 2019; Dumitrache & Yalin 2020). Here, we experimentally investigate the shock wave’s contribution to the vortex ring vorticity generation. We employ high-speed schlieren visualization and image processing methods to measure the shock properties and a model to calculate the vorticity based on these shock properties. We compare the estimated vorticity to measurements from stereoscopic particle image velocimetry (S-PIV) from prior work (Singh *et al.* 2020b) and explore how the shock wave accounts for the vorticity in the vortex rings that drive cooling of the hot gas kernel.

## 2. Vorticity generation due to a curved shock

Vorticity can be generated at a boundary and within a fluid due to baroclinicity or body forces. The vorticity transport equation is given as:

$$\frac{D\vec{\omega}}{Dt} = (\vec{\omega} \cdot \nabla)\vec{u} - \vec{\omega}(\nabla \cdot \vec{u}) + \frac{1}{\rho^2}\nabla\rho \times \nabla p + \nabla \times \left(\frac{1}{\rho}\nabla \cdot \tau\right) + \nabla \times \vec{f} \quad (2.1)$$

where  $\vec{\omega}$  is vorticity,  $\vec{u}$  is the velocity,  $\rho$  and  $p$  are the density and pressure, respectively,  $\tau$  is the viscous stress tensor and  $\vec{f}$  is a body force. The first two terms on the right-hand side represent changes in vorticity due to vortex stretching and compressibility effects, respectively. The third term represents the generation of vorticity due to misalignment of pressure and density gradients, which leads to baroclinic torque. The last two terms represent the diffusion of vorticity due to viscosity and the generation of vorticity due to a body force. In a compressible flow, such as the early stages ( $< 20 \mu\text{s}$ ) of the flow induced by a spark discharge, if we neglect body forces and use the simplifying assumption that the flow is inviscid, we can neglect the last two terms in equation 2.1.

In spark discharges, the primary source of vorticity is baroclinic torque, which is hypothesized to arise from the non-uniform velocity of the shock wave (Dumitrache *et al.* 2019; Wang *et al.* 2020), which results in a curved shock. The generation mechanism of vorticity behind a curved shock has been explained using a purely dynamic approach by Hayes (Hayes 1957), who shows that the vorticity generated due to a curved shock is dependent only on the magnitude of the tangential component of the shock velocity. Other work used Crocco’s theorem to arrive at the same result as Hayes for vorticity jump across a curved shock (Truesdell 1952; Lighthill 1957; Hayes & Probstein 1959). These works show that the non-uniformity in shock strength generates non-uniform entropy behind a curved shock, resulting in an entropy gradient along the shock, which is responsible for vorticity generation. However, these studies are restricted to steady flows due to Crocco’s vorticity law’s inherent assumption, a restriction that is not necessary for Hayes’ derivation.

The schematic in figure 1 shows a slice of the curved shock generated by a spark discharge in cylindrical coordinates. The middle portion of the shock is approximately cylindrical and has been shown, via CFD simulations, to be stronger than the portions of the shock closer to the electrodes (Bane *et al.* 2015). The difference in the strength of the shock along its length results in pressure and density gradients behind the shock that are misaligned, leading to

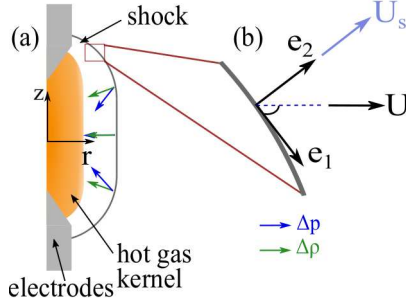


Figure 1: Schematic of shock induced by a spark discharge showing (a) the curved shock wave in cylindrical coordinates and the misalignment of pressure and density behind the shock due to non-uniform shock strength; (b) the local coordinate system for a shock segment with normal shock velocity  $U_s$  and horizontal component of shock velocity  $U$ .

baroclinicity (Hornung 1998; Bershader 1995). The misalignment in the density and pressure gradients occurs in the regions where the shock is curved, with almost no misalignment in the center of the gap where the shock wave is mostly straight.

According to Hayes (Hayes 1957), the vorticity jump across this unsteady, axisymmetric, curved shock, generated under quiescent flow conditions, is given by:

$$\omega = -\frac{\partial U_s}{\partial e_1} (\epsilon - 1)^2 \epsilon^{-1} \quad (2.2)$$

where  $U_s$  is the normal shock velocity. The tangential gradient  $\frac{\partial U_s}{\partial e_1}$  can be expressed in terms of the tangential shock velocity,  $U \cos \sigma$ , and shock curvature,  $\kappa$ , hence equation 2.2 becomes:

$$\omega = -U \cos \sigma \kappa (\epsilon - 1)^2 \epsilon^{-1} \quad (2.3)$$

where  $\sigma$  is the angle the shock makes with the horizontal. The local shock curvature ( $\kappa = \frac{d\sigma}{de_1}$ ) is negative for the convex surface of the spark induced shock. The shock strength, measured as the density ratio  $\epsilon$ , is the ratio of the density behind the shock,  $\rho_s$ , to the density ahead of the shock  $\rho_\infty$ :

$$\epsilon = \frac{\rho_s}{\rho_\infty} = \frac{(\gamma + 1) M_n^2}{(\gamma - 1) M_n^2 + 2} \quad (2.4)$$

where  $\gamma$  is the ratio of specific heats, which assuming a perfect gas with constant specific heats, is taken to be 1.4. The normal shock Mach number,  $M_n$ , is calculated as  $\frac{U_s}{a}$  where  $a$  is the speed of sound in the ambient air, taken to be 343 m/s. Therefore, to calculate the shock-generated vorticity, the model (equation 2.3-2.4) requires the density ratio and the tangential shock velocity estimated from the shock Mach number, and the shock curvature and shock angle obtained from the shock profile. The next section details the experimental measurements capturing the shock wave and the procedure to estimate these parameters.

### 3. Experimental methods and techniques

The shock wave induced by a single spark discharge was captured using schlieren imaging for energy values ranging from 4.3 to 5.3 mJ, resulting in a total of 10 distinct experiments. Each spark discharge was generated using a nanosecond high voltage pulser in a 5 mm gap between two ceriated-tungsten electrodes with cone-shaped tips. Details on the plasma generation are given in prior work (Singh *et al.* 2020a). The parameters needed to calculate

the vorticity jump across the shock were extracted from the first image of the shock after it had separated from the hot gas kernel, approximately  $3.5 \mu\text{s}$  after the spark.

### 3.1. Schlieren Imaging

A Z-type schlieren set-up was used to image the spark induced shock wave. The system consisted of a 150 W xenon arc lamp (Newport 66907) and a 60 mm aspheric condenser lens to create a point light source. Two concave mirrors 152.4 mm in diameter and with a focal length of 3.05 m, were used to collimate the light beam then converge it onto a knife edge. The camera was set to a frame rate of 700,000 fps ( $\sim 1.4 \mu\text{s}$  between frames) at a resolution of  $64 \times 128$  pixels corresponding to a field of view of approximately  $5 \times 10$  mm and magnification of 0.08 mm/pixel.

### 3.2. Processing metrics and calculation of parameters

The ultra-high-speed recording leads to high image noise due to low exposure times and low spatial resolution due to camera hardware limitations. Additionally, the derivative calculations needed to estimate the shock parameters further amplify the noise and deteriorate the measurements due to large random errors. Therefore, a correlation-based data processing procedure was employed to estimate the shock parameters from the schlieren images to achieve an optimal tradeoff between the measurements' systematic and random errors.

The processing steps used to model the shock-generated vorticity from the schlieren images are summarized in figure 2. Each schlieren experiment captured 990 pre-triggered images of the background and 10 images after the spark discharge. The mean of the pre-triggered images was subtracted from the first image of the shock after it had separated from the hot gas kernel, approximately  $3.5 \mu\text{s}$  after the spark. The background-subtracted image was flipped along the center of the electrode gap and averaged. The new shock image was used to detect the shock outline and calculate the shock velocity.

#### 3.2.1. Shock outline detection

To detect the shock outline, each row of pixels in the shock image was cross-correlated with the first row of pixels containing the shock by first replicating the single row of pixels to create a 2D intensity map which was 16 pixels in height (figure 2(a)). We applied a 50% Gaussian window (Eckstein & Vlachos 2009b) to the 2D map of intensities and cross-correlated the intensities using Robust Phase correlation (Eckstein & Vlachos 2009a) to determine the displacement of the shock and define the shock outline. The ensemble cross-correlation was calculated along the columns of each 2D map, and a least-squares Gaussian fit to the cross-correlation peak was used to obtain the subpixel location of the shock profile along the horizontal direction for each row of pixels. We then smoothed the shock profile using a moving linear regression.

We used the shock profile (figure 2(b)) to calculate the shock angle and shock curvature. The shock angle (figure 2(c)) was calculated as the arctangent of the derivatives of the  $r$  and  $z$  locations of the shock outline, with the derivatives calculated using a 4th order compact noise optimized Richardson extrapolation scheme (Etebari & Vlachos 2005). The shock angle and the Euclidean distance between velocity grid points were used to calculate the shock curvature (figure 2(d)).

#### 3.2.2. Shock velocity calculation

To determine the normal shock velocity, we cross-correlated successive shock images recorded at  $3.5 \mu\text{s}$  and  $4.9 \mu\text{s}$  after the spark. The interrogation windows had a height of 16 pixels, containing 16 points of the shock outline and the orientation of the window was

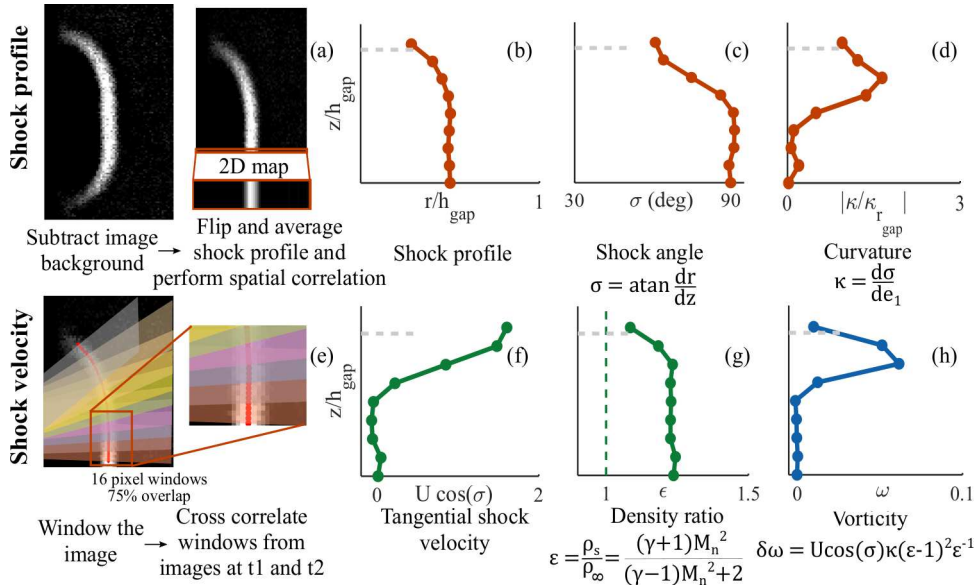


Figure 2: Processing steps to calculate the vorticity jump across a shock wave using schlieren images. The z-location of the electrode tip is shown as a grey dashed line.

determined using the slope of the line perpendicular to the center shock point in the window (figure 2(e)). We applied a 75% overlap and a 50% Gaussian window to the original window size, resulting in a window resolution of 8 pixels in height and grid resolution of 2 pixels (0.16 mm). The intensities in the same window from the first and second time steps were cross-correlated using Robust Phase correlation to determine the normal shock velocity. The ensemble of the cross-correlation plane was calculated, and a least-squares Gaussian fit to the cross-correlation peak was used to determine the subpixel shock displacement.

### 3.2.3. Shock-generated vorticity calculation

The tangential shock velocity (figure 2(f)), shock angle, shock curvature and density ratio (figure 2(g)) were used to calculate the spatial variation of the shock-generated vorticity (figure 2(h)) according to equation 2.3. All results were non-dimensionalized using the induced velocity and density behind the shock, calculated according to (Jones *et al.* 1968; Singh *et al.* 2018), and the characteristic length scale was taken to be half the electrode gap distance (2.5 mm). Further details on the non-dimensionalization can be found in prior work (Singh *et al.* 2020a).

### 3.3. Uncertainty quantification

Experimental uncertainties in the displacement field used to estimate both the shock profile and the shock velocity were calculated using the moment of correlation (MC) method (Bhattacharya *et al.* 2018), then propagated through the shock-generated vorticity calculations using the Taylor series-based propagation method (Coleman & Steele 2009). The maximum uncertainties in the calculation of  $r$  and  $z$  for the shock profile were 0.03 mm and 0.04 mm, respectively, corresponding to 1.2% and 1.6% of the half-gap distance (2.5 mm). The maximum uncertainties for the shock velocity calculation were 20 m/s, corresponding to 5% of the maximum velocity, 412 m/s. The modeled vorticity jump uncertainties ranged from 20% to 60% of the vorticity jump value, with the majority (~70%) of the vorticity jump uncertainties being less than 40% of their respective vorticity jump values.

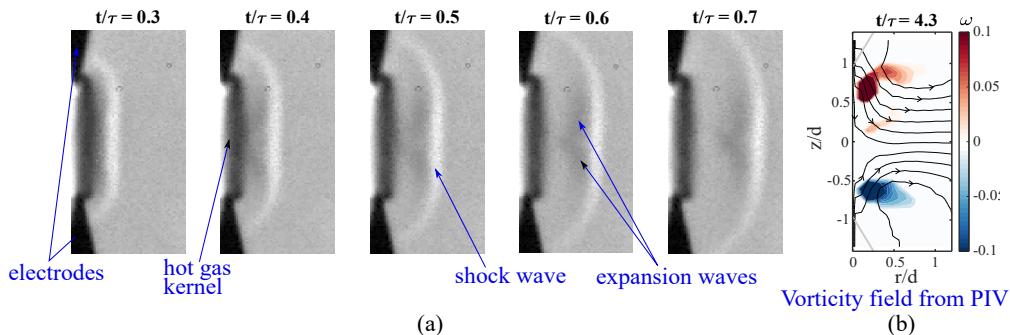


Figure 3: (a) Time evolution of a spark induced shock wave (4.9 mJ energy,  $\tau=14 \mu\text{s}$ ) in a 5mm gap. (b) Vorticity field from prior work for a similar spark (5 mm gap, 4.8 mJ,  $\tau=14.1 \mu\text{s}$ ) showing a pair of vortex rings near the electrode tips (Singh *et al.* 2020b).

## 4. Results and discussion

### 4.1. Shock wave induced by spark discharge

An example of the flow field induced after a single spark discharge generated under quiescent conditions in a 5 mm electrode gap and corresponding to a deposited energy of 4.8 mJ is presented in figure 3(a). The flow field shown spans approximately  $10 \mu\text{s}$  and is comprised of a cylindrical hot gas kernel and a shock wave, trailed by expansion waves. In the first snapshot at  $\frac{t}{\tau} = 0.3$ , the shock wave has completely separated from the induced hot gas kernel. The shape of the shock wave resembles that shown in the schematic in figure 1, where the parts of the shock closest to the electrodes are curved, while the parts near the center of the electrode gap are cylindrical. The normal Mach number along the shock ranges between 1.05 to 1.2, with the normal shock velocity decreasing along the length of the shock from the center of the electrode gap out toward the electrode tips. The Mach number in the center region of the gap remains approximately constant at 1.2. The shape of the Mach number profile (not shown) follows that of the shock outline and resembles the density jump profile shown in figure 4(d).

The first time step shown in figure 3(a) is used to calculate the vorticity jump across the shock because the progressive reduction in the magnitude and non-uniformity of the shock velocity will lead to negligible vorticity production at later times. The shock-generated vorticity estimated using the model is compared to the vorticity calculated directly from a separate set of S-PIV experiments from prior work (Singh *et al.* 2020b). An example of the vorticity field induced at later times is shown in figure 3(b), where a pair of vortex rings are generated near the electrode tips.

### 4.2. Vorticity estimation based on shock curvature

The spatial profiles of the parameters used to calculate the vorticity jump across the spark induced shock are shown in figure 4 and normalized by their maxima. The profiles calculated from each schlieren experiment are overlaid in the same figure. The orange profiles show quantities calculated using the shock profile, the green profiles are quantities calculated using a combination of the shock profile and shock velocity, and the blue profiles show the vorticity.

The shock outlines in figure 4(a) are seen to be curved in all tests, with the curvature in figure 4(b) being close to zero near the center of the gap and highest near the electrodes (the  $z$ -location of the electrode tip is shown by the gray dashed line). The tangential shock velocity (figure 4(c)) increases monotonically from the center of the shock ( $z = 0$ ) to the ends of the shock near the electrodes. The density ratio term (figure 4(d)), which represents

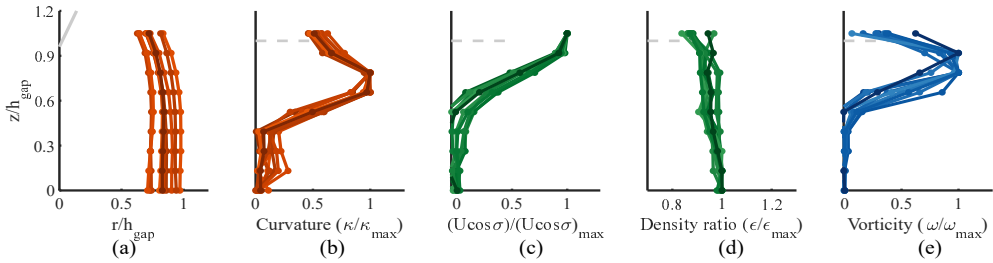


Figure 4: Normalized spatial variation of shock properties: (a) shock profile, (b) curvature, (c) tangential velocity, (d) density ratio, and (e) vorticity jump across the shock.

the shock's strength, is almost constant near the center region of the shock and decreases as we move closer to the electrodes, corresponding to a decrease in the normal Mach number. The density ratio profile is the same as that of the normal shock velocity (not shown), both roughly resembling the shock profile. Combining the first 4 terms into equation 2.3 gives the final vorticity jump across the length of the shock (figure 4(e)), with negligible vorticity generated near the center of the gap and the peak vorticity being generated in the region of highest curvature.

#### 4.3. Comparison of shock-estimated vorticity to experimental results from S-PIV

For all the experiments, the peak vorticity is determined for comparison to the S-PIV results from prior work. The shock parameters calculated from the schlieren and S-PIV measurements are plotted against the analytic, normalized pressure gradient across the shock, calculated from the energy deposited in the electrode gap. This allows for comparing two independent measurements while demonstrating the effect of the analytic shock strength and energy deposited in the gap on the different parameters. The analytic, normalized pressure gradient, like the density ratio calculated in the previous section, is also a measure of the strength of the shock wave, although the density ratios calculated in this study are all obtained directly from the schlieren images. The analytic, normalized pressure gradient and analytic shock strength will be used interchangeably.

The analytic, normalized pressure gradient across the shock is calculated according to Jones et al. (Jones *et al.* 1968) as:

$$\frac{p_2 - p_1}{p_1} = \frac{2\gamma}{\gamma + 1} (M_1^2 - 1) = \frac{2\gamma}{\gamma + 1} \frac{0.4503}{\left(1 + 4.803 \left(\frac{r}{R_0}\right)^2\right)^{\frac{3}{8}}} - 1 \quad (4.1)$$

where the subscripts 1 and 2 represent conditions upstream and downstream of the shock, respectively, and  $r$  is the radial distance at which flow properties behind the shock are measured. In the present context, the radial distance is half the electrode gap distance (2.5 mm). The variable  $R_0$  is the characteristic radius determined by the initial conditions and is given by:

$$R_0 = \left[ \frac{4E_0}{3.94\gamma p_1} \right]^{\frac{1}{2}} \quad (4.2)$$

where  $E_0$  is the electrical energy deposited by the plasma per unit length of the electrode gap. The analytic, normalized pressure gradient (analytic shock strength) increases with an increase in electrical energy deposited in the gap.

Figure 5 shows the peak vorticity and peak curvature locations and the shock curvature,

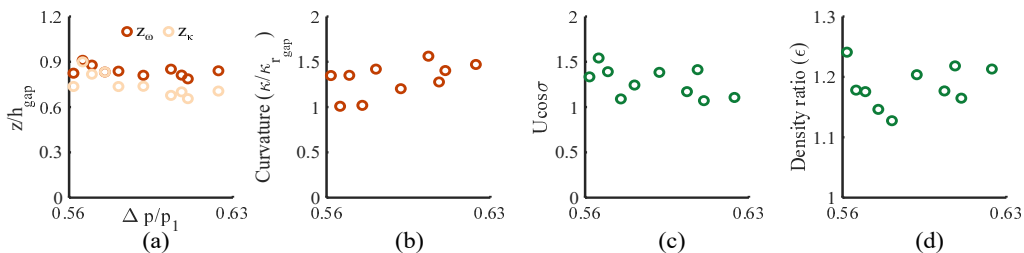


Figure 5: (a) The locations of peak vorticity and peak shock curvature and (b) shock curvature, (c) tangential velocity and (d) density ratio used to calculate the maximum shock-generated vorticity as a function of the analytic, normalized pressure gradient.

tangential velocity, and density ratio which determine the peak vorticity as a function of the analytic shock strength. The peak vorticity location and the tangential shock velocity at peak vorticity show no clear dependence on the analytic shock strength. The peak vorticity location is roughly the same for almost all experiments, occurring near the peak curvature location. The shock curvature at the locations of peak vorticity show a weak dependence on the analytic shock strength, while the density ratio increases with the analytic shock strength, as expected.

These results show that the density ratio estimates calculated from the schlieren images can capture the expected increase in density ratio, which is a measure of the experimentally calculated shock strength, with an increase in the electrical energy deposited. We also demonstrate using these results that stronger shocks tend to have higher maximum curvature (smaller radius of curvature) than weaker shocks. The curvature values in the region of peak vorticity range from approximately 1 (radius of curvature of half the electrode gap) to approximately 1.7.

The peak shock-generated vorticity jump obtained from the schlieren images is compared to the mean vorticity within the vortex rings from S-PIV experiments described in prior work (Singh *et al.* 2020b). The velocity field obtained from S-PIV was flipped and averaged along the  $z = 0$  axis to obtain a single coherent structure representing the vortex ring's core in each experiment. The peak shock-generated vorticity and the mean vorticity calculated in the vortex rings are compared in figure 6. The median values are 0.046 and 0.05 from the shock and vortex rings, respectively. This shows that the vorticity from the model based on shock curvature and the vorticity in the vortex rings are statistically equivalent over the range of experiments performed in this study. This suggests that the shock curvature is a likely source of the vorticity observed in the vortex rings at later times.

However, there is considerable scatter in the vorticity values and a negligible dependence on the analytic pressure gradient. Further, the S-PIV and schlieren measurements are from different experiments, and some of the variability is likely due to the stochastic nature of the spark discharge as well as the high uncertainties in the shock-generated vorticity estimates. Additionally, the schlieren measurements are taken at approximately  $3 \mu\text{s}$ , whereas the first PIV measurements are taken at approximately  $30 \mu\text{s}$ , further explaining the model and experiment's mismatch and limiting a direct comparison.

## 5. Conclusions

The flow field induced by a single spark discharge consists of a curved shock wave that propagates radially outward, leaving behind a region of hot gas and vortex ring(s) which drive the cooling and expansion of the hot gas kernel. We use schlieren experiments to capture the shock and develop an image-processing procedure that mitigates the effects of

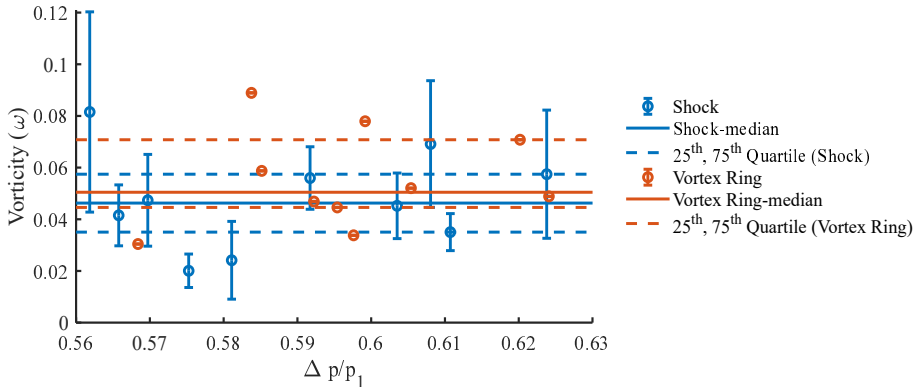


Figure 6: Comparison between the non-dimensionalized peak vorticity estimated from the schlieren images with a curved shock model and mean vorticity from PIV measurements.

high image noise and low spatial resolution to extract the shock properties. We use the shock properties to estimate the shock-generated vorticity and compare it to the vortex ring vorticity.

This work shows that the shock profile is approximately cylindrical in the center of the gap, with nearly zero shock curvature which increases towards the electrodes and reaches peak curvatures of approximately  $\frac{\kappa}{\kappa_{gap}} = 1.7$ . The normal shock Mach number is highest near the center of the gap, close to Mach 1.2, and decreases near the electrodes to approximately 1.05. The peak values of both the shock Mach number and curvature increase with the analytic pressure gradient, which is related to the electrical energy deposited in the gap. The magnitude of the tangential velocity increases along the shock, and its peak value shows no clear dependence on the analytic pressure gradient. The shock-generated vorticity is close to zero at the center of the gap and increases along the shock towards the electrode tips. The highest vorticity is observed in the regions of the highest shock curvature, with the peak vorticity showing no clear dependence on the analytic pressure gradient. These results are similar to CFD simulations (Dumitrache *et al.* 2019) showing the presence of vortices in the region where the shock wave curvature is highest.

The shock-generated vorticity is compared to the vorticity from experimental S-PIV results from previous work (Singh *et al.* 2020b) with both shown to be statistically equivalent. This suggests that the shock wave induced at early times ( $< 20 \mu\text{s}$ ) likely generates the vorticity in the vortex rings that control the cooling and dynamics of the hot gas kernel at later times ( $> 50 \mu\text{s}$ ). The work is limited in that the schlieren and PIV measurements were non-simultaneous, and the time at which the vorticity is calculated from the model is an order of magnitude lower than the first snapshot of vorticity from the PIV experiments.

We show that the vorticity induced by a spark discharge may be approximated from the shock curvature and velocity using schlieren experiments and used to estimate the strength of the vortex rings, having implications in the late stages of the flow field. In pin-to-pin discharges, knowing the vortex rings' strength can inform the cooling rate (Singh *et al.* 2020a,b), while in laser sparks, the relative difference in the strength of the induced vortex rings informs the direction of ejection (Dumitrache & Yalin 2020; Wang *et al.* 2020). These findings underscore that peak vorticity is generated at the location of peak curvature and controlling the shock strength and location of peak curvature affects the late flow dynamics.

**Acknowledgements.** This material is based upon work supported by the US Department of Energy, Office of Science, Office of Fusion Energy Sciences under Award No. DE-SC0018156.

**Declaration of interests.** The authors report no conflict of interest.

## REFERENCES

- BANE, SALLY P.M. M, ZIEGLER, JACK L. & SHEPHERD, JOSEPH E. 2015 Investigation of the Effect of Electrode Geometry on Spark Ignition. *Combustion and Flame* **162** (2), 462–469.
- BERSHADER, D 1995 Compressible vortices. In *Fluid vortices*, pp. 291–316. Springer.
- BHATTACHARYA, SAYANTAN, CHARONKO, JOHN J & VLACHOS, PAVLOS P 2018 Particle image velocimetry (PIV) uncertainty quantification using moment of correlation (MC) plane. *Measurement Science and Technology* **29** (11), 115301.
- COLEMAN, HUGH W. & STEELE, W GLENN 2009 *Experimentation, Validation, and Uncertainty Analysis for Engineers*. Hoboken: John Wiley & Sons, Inc.
- DUMITRACHE, CIPRIAN, GALLANT, ARNAUD, MINESI, NICOLAS, STEPANYAN, SERGEY, STANCU, GABI D. & LAUX, CHRISTOPHE O. 2019 Hydrodynamic regimes induced by nanosecond pulsed discharges in air: Mechanism of vorticity generation. *Journal of Physics D: Applied Physics* **52** (36), 364001.
- DUMITRACHE, CIPRIAN & YALIN, AZER P 2020 Gas dynamics and vorticity generation in laser-induced breakdown of air. *Optics Express* **28** (4).
- ECKSTEIN, ADRIC & VLACHOS, PAVLOS P. 2009a Digital particle image velocimetry (DPIV) robust phase correlation. *Measurement Science and Technology* **20** (5).
- ECKSTEIN, ADRIC C. & VLACHOS, PAVLOS P. 2009b Assessment of advanced windowing techniques for digital particle image velocimetry (DPIV). *Measurement Science and Technology* **20** (7), 075402.
- ETEBARI, A & VLACHOS, P 2005 Improvements on the accuracy of derivative estimation from DPIV velocity measurements. *Experiments in Fluids* pp. 39(6), 1040–1050.
- HAYES, WALLACE D. 1957 The vorticity jump across a gasdynamic discontinuity. *Journal of Fluid Mechanics* **2** (6), 595–600.
- HAYES, W. D. & PROBSTEIN, R. F. 1959 General Considerations. In *Hypersonic flow theory*, chap. 1, pp. 1–29. New York and London: Academic Press.
- HORNUNG, H. G. 1998 Gradients at a curved shock in reacting flow. *Shock Waves* **8** (1), 11–21.
- JONES, D.L., GOYER, G.G. & PLOOSTER, M.N. 1968 Shock Wave from a Lightning Discharge. *Journal of Geophysical Research* **73** (10).
- LEFKOWITZ, JOSEPH K. & OMBRELLO, TIMOTHY 2017 An exploration of inter-pulse coupling in nanosecond pulsed high frequency discharge ignition. *Combustion and Flame* **180**, 136–147.
- LIGHTHILL, M 1957 *Dynamics of a dissociating gas, Part {1}. Equilibrium flow*, vol. 2.
- PHUOC, TRAN X. 2006 Laser-induced spark ignition fundamental and applications. *Optics and Lasers in Engineering* **44** (5), 351–397.
- PICONE, J. M. & BORIS, J. P. 1983 Vorticity generation by asymmetric energy deposition in a gaseous medium. *Physics of Fluids* **26** (2), 365–382.
- PILLA, GUILLAUME L., LACOSTE, DEANNA A., VEYNANTE, DENIS & LAUX, CHRISTOPHE O. 2008 Stabilization of a swirled propane-air flame using a nanosecond repetitively pulsed plasma. *IEEE Transactions on Plasma Science* **36** (4 PART 1), 940–941.
- RAIZER, YURI, P. 1991 *Gas discharge physics*.
- RAJENDRAN, LALIT K., SINGH, BHAVINI, VLACHOS, PAVLOS P. & SALLY, P M 2020 Filamentary Surface Plasma Discharge Flow Length and Time Scales. *arXiv*, arXiv: 2010.08446.
- SINGH, BHAVINI, RAJENDRAN, LALIT K., GIARRA, MATTHEW, VLACHOS, PAVLOS P. & BANE, SALLY P.M. 2018 Measurement of the flow field induced by a spark plasma using particle image velocimetry. *Experiments in Fluids* **59** (12).
- SINGH, BHAVINI, RAJENDRAN, LALIT K., GUPTA, PRATEEK, SCALO, CARLO, VLACHOS, PAVLOS P. & BANE, SALLY P. 2019 Experimental and Numerical Study of Flow Induced by Nanosecond Repetitively Pulsed Discharges. In *AIAA SciTech Forum*, pp. 1–15.
- SINGH, BHAVINI, RAJENDRAN, LALIT K, VLACHOS, PAVLOS P & BANE, SALLY P.M. 2020a Two regime cooling in flow induced by a spark discharge. *Physical Review Fluids* **5** (1), 14501.
- SINGH, BHAVINI, RAJENDRAN, LALIT K, ZHANG, JIACHENG, VLACHOS, PAVLOS P & BANE, SALLY P.M. 2020b Vortex rings drive entrainment and cooling in flow induced by a spark discharge. *Physical Review Fluids* **5**, 114501, arXiv: 2007.11065.
- TRUESDELL, C. 1952 On Curved Shocks in Steady Plane Flow of an Ideal Fluid. *Journal of the Aeronautical Sciences* **19** (12), 826–828.
- WANG, JONATHAN M, BUCHTA, DAVID A & FREUND, JONATHAN B 2020 Hydrodynamic ejection caused by laser-induced optical breakdown. *Journal of Fluid Mechanics* **888**.